RSC Advances

PAPER

View Article Online
View Journal | View Issue

Cite this: *RSC Adv.*, 2026, **16**, 22021

Biohybrid nanostructured ceria/glucose oxidase electrodes enabling enzyme glucose oxidation with pseudocapacitive charge buffering

Mohamed Mohamedi * and Mouna Moumene

Biohybrid nanostructured electrodes that integrate redox enzymes with defect-engineered inorganic supports offer a promising route to couple bioelectrocatalysis with interfacial charge buffering. Here, nanostructured cerium oxide (CeO_2) films with tunable oxygen-vacancy concentrations were deposited by pulsed laser deposition under controlled atmospheres and subsequently functionalized with glucose oxidase (GOx) to form CeO_2/GOx electrodes. Control of the deposition environment enabled systematic tuning of ceria nanostructure, crystallinity, and Ce^{3+}/Ce^{4+} ratios, as confirmed by Raman spectroscopy and X-ray photoelectron spectroscopy (XPS). XPS further confirms enzyme immobilization through the presence of amide/amine nitrogen from the GOx backbone and heterocyclic nitrogen associated with the flavin adenine dinucleotide (FAD) cofactor, indicating preservation of the redox-active center at the ceria interface. Electrochemical measurements show that pristine CeO_2 films exhibit predominantly pseudocapacitive behavior and no measurable response toward glucose oxidation, whereas CeO_2/GOx electrodes display distinct catalytic redox features in the presence of glucose. The formal potential of the surface-confined redox couple is scan-rate independent and closely matches that of the FAD/$FADH_2$ couple, consistent with electronic communication between GOx and the ceria support. In addition to bioelectrocatalytic activity, CeO_2/GOx electrodes exhibit measurable charge-storage capability arising from the combined contribution of Ce^{3+}/Ce^{4+} redox processes and reversible FAD cycling. These results demonstrate the feasibility of coupling enzymatic redox activity with pseudocapacitive charge buffering in oxide-based biohybrid electrodes, providing a versatile platform for future bioelectrochemical energy conversion and enzymatic biofuel cell applications.

Received 6th February 2026
Accepted 22nd April 2026

DOI: 10.1039/d6ra01081d

rsc.li/rsc-advances

1. Introduction

Glucose holds significant importance in bioelectrochemical technologies, particularly in enzymatic electrodes for biofuel cells and in electrochemical platforms for fundamental studies of enzyme–electrode interfaces.[1,2] Glucose oxidase (GOx) enzyme is widely employed due to its high catalytic activity and operational stability at near-neutral pH.[3] Typically, the redox centers within GOx are nestled within the protein matrix, spatially distant from the electrode. This spatial arrangement hinders direct electrical contact between the protein/enzyme and the electrode.[4]

For effective catalytic function, GOx relies on a cofactor called flavin adenine dinucleotide (FAD), which is tightly bound and deeply embedded approximately 15 Å below the protein surface.[5] This center undergoes reduction to $FADH_2$ upon interaction with glucose. Subsequently, $FADH_2$ is reoxidized to FAD either by molecular oxygen, resulting in the formation of hydrogen peroxide, or by the oxidizing member of a redox couple. However, due to the insulation of GOx's redox center from the conductive support by the protein matrix, achieving direct electron transfer (DET) between GOx and electrode remains challenging.[6] This DET (direct electron transfer) enables electrons to shuttle between the GOx redox center and the electrode.

In this context, metal oxide nanostructures offer an alternative approach to establishing enzyme–electrode electronic coupling. Cerium oxide (CeO_2) is an especially attractive candidate due to its low cost, chemical stability, biocompatibility, rich redox chemistry and a high surface-to-volume ratio, similar to many other nanostructured materials as noted by Rahman *et al.*[7] et Ball *et al.*[8] Furthermore, cerium oxide exhibits potential antioxidant properties, effectively combating a broad spectrum of harmful intracellular reactive oxygen species. In various biological domains, ranging from bioanalysis to biomedicine, drug delivery, and biostructures, cerium oxide nanoparticles have garnered significant attention.[9] Notably, nanoscale ceria has showcased remarkable superoxide dismutase mimetic and catalase mimetic activities, highlighting its multifaceted utility.[10,11] The notably high isoelectric point

Institut National de la Recherche Scientifique (INRS)-Énergie, Matériaux et Télécommunications (EMT), 1650 Boulevard Lionel Boulet, Varennes, Québec, J3X 1P7, Canada. E-mail: Mohamed.Mohamedi@inrs.ca

(IEP ≈ 9.2) of CeO_2 offers a distinct advantage for immobilizing enzymes with lower IEP values, such as GOx with an IEP of approximately 4.2.[12] The positively charged surface of CeO_2 provides an ideal platform for the negatively charged GOx, fostering electrostatic interactions that aid in preserving GOx bioactivity. Additionally, CeO_2 demonstrates remarkable oxygen storage and release capabilities with minimal lattice distortion, facilitated by reversible redox processes involving the cerium atom transitioning from Ce^{4+} to Ce^{3+}.[13] This inherent property allows the network of Ce redox centers to effectively "wire" the reaction center of the protein to the current collector (electrode), thereby enhancing rapid electron shuttling with the FAD redox center of GOx. In a previous brief communication, the synthesis of nanoscale ceria thin films *via* the pulsed laser deposition (PLD) method was introduced, conducted within a vacuum environment. These films exhibited a notably smooth surface, positioning them as promising candidates for facilitating DET, as outlined in prior research.[14] Notably, the PLD technique offers distinct advantages over alternative deposition methodologies, particularly in enabling the growth of layers with diverse surface morphologies, a capability not readily achievable through other techniques.[15] This flexibility is achieved through the introduction of inert or reactive gas into the deposition chamber and subsequent adjustment of pressure, allowing for the controlled growth of films with varying levels of porosity.[16,17]

In this work, we investigate how the surface morphology of CeO_2 thin films, tailored *via* pulsed laser deposition under controlled atmospheres (vacuum, He and O_2), governs enzyme–electrode interactions and glucose electrooxidation. In addition, these atmospheres were also chosen to systematically tune oxygen vacancy concentration and the Ce^{3+}/Ce^{4+} ratio, which are key parameters governing the redox behavior and electrochemical properties of CeO_2. The resulting nanostructured films are analyzed using TEM, Raman spectroscopy, and X-ray photoelectron spectroscopy (XPS) to establish correlations between structural, chemical, and interfacial properties. The bioelectrochemical behavior of the CeO_2/glucose oxidase (GOx) interface is then evaluated by cyclic voltammetry in phosphate buffer, revealing the impact of morphology on electron transfer and catalytic response.

Beyond material characterization, this study focuses on the functional integration of nanostructured CeO_2 within a bioelectrochemical system. Specifically, we demonstrate a biohybrid CeO_2/GOx interface capable of enzyme-driven glucose electrooxidation coupled with intrinsic pseudocapacitive charge buffering. By systematically tuning the film morphology, we elucidate the interplay between enzyme–electrode electronic coupling, charge storage behavior, and catalytic performance. These findings provide new mechanistic insight into how nanostructured redox-active oxides can serve as electronically coupled interfaces that promote direct electron transfer-like processes, rather than functioning as classical mediated electron transfer systems.

To further position this work within the current literature, it is important to emphasize that conventional glucose oxidase (GOx) electrodes typically rely on mediated electron transfer (MET), while ceria-based materials have primarily been explored for sensing or structural applications, and pseudocapacitive oxides have been investigated independently of enzymatic catalysis. In contrast, the present study demonstrates the integration of enzymatic redox activity with intrinsic pseudocapacitive charge buffering within a single biohybrid interface. To the best of our knowledge, such coupling between bioelectrocatalysis and oxide-based pseudocapacitive charge storage has not been previously reported. It should be noted that the present study is primarily focused on elucidating fundamental bioelectronic coupling mechanisms rather than on the optimization of biosensor performance metrics such as enzyme loading, long-term stability, or device reproducibility.

2. Materials and methods

2.1. Materials synthesis

CeO_2 was synthesized *via* PLD at room temperature, using a pulsed KrF excimer laser with a wavelength (λ) of 248 nm, a pulse width of 17 ns, and a repetition rate of 50 Hz. The deposition process was carried out onto a carbon paper substrate (CP, Toray). A high-purity CeO_2 target (99.99%, Kurt J. Lesker Co.) was employed for deposition, with a laser fluence of 4 J cm^{-2} and 20 000 laser pulses. To achieve diverse surface morphologies, depositions were conducted under four distinct background pressures: vacuum, 0.5 Torr of helium, 2 Torr of helium, and 10 mTorr of oxygen. During the deposition process, the target-to-substrate distance was maintained at 50 mm. Before deposition, the PLD chamber underwent evacuation using a turbo pump (2×10^{-5} Torr), followed by the introduction of helium or oxygen into the deposition chamber. Throughout deposition, the CeO_2 target underwent continuous rotation and translation to ensure uniform ablation across its entire surface. Additional details regarding the PLD setup can be found elsewhere.[18] The samples in this study are designated as follows: $(CeO_2)_{UV}$, $(CeO_2)_{0.5THe}$, $(CeO_2)_{2THe}$, and $(CeO_2)_{10mTO2}$, representing CeO_2 films prepared under vacuum, 0.5 Torr of helium, 2 Torr of helium, and 10 mTorr of oxygen, respectively.

All films were deposited under strictly controlled and reproducible PLD conditions, and consistent electrochemical behavior was observed across independently prepared samples.

2.2. Characterization

The surface morphology of the freshly prepared samples was evaluated using TEM with a JEOL-JEM-2100F operating at 200 kV. For surface composition analysis, XPS was employed with a VG Escalab 220i-XL equipped with an Al Kα source (1486.6 eV). The anode operated at 10 kV and 20 mA, while the pass energy of the analyzer was maintained at 20 eV. All samples underwent analysis with a spot size of 250 × 1000 μm, positioned approximately at the center of each sample. Initially, a survey spectrum spanning from 0 to 1300 eV was acquired, followed by the acquisition of higher-resolution multiplex scan spectra for Ce 3d, O 1s, N 1s, and C 1s core levels. Elements quantification was performed using CasaXPS software (Casa Software Ltd), involving fitting of the core level spectra following Shirley

background removal. The C 1s core level peak at 284.6 eV, attributed to hydrocarbon contaminants on the surface, served as an internal reference for calibration. Notably, all spectra were recalibrated relative to the C 1s core level peak originating from adventitious carbon contamination. Micro-Raman spectroscopy was conducted utilizing the 514.5 nm (2.41 eV) laser radiation emitted by an Ar^+ laser, with circular polarization. The laser beam was focused onto the sample, achieving a spot size of 1 μm in diameter, utilizing a Renishaw Imaging Microscope WireTM for micro-Raman spectroscopy.

2.3. Enzyme immobilization

To immobilize GOx on CeO_2, a physisorption method was utilized. In this process, CeO_2 samples were immersed in a phosphate buffer solution (PBS) with a pH of 7.2, sourced from Sigma-Aldrich, Canada Ltd This PBS solution contained 15 mg mL^{-1} of GOx derived from Aspergillus niger (168 800 units/G, Sigma-Aldrich Canada Ltd). Subsequently, the samples were stored overnight at 4 °C in a refrigerator before further use.

2.4. Electrochemical measurements

The DET characteristics between GOx and CeO_2 substrates were investigated *via* CV analysis. This was conducted in a deaerated PBS solution with a pH of 7.2, both in the presence and absence of a glucose solution (D-(+)-glucose, ACS reagent grade, sourced from Sigma-Aldrich). All electrochemical measurements were carried out at room temperature using a three-electrode cell setup. The reference electrode and counter electrode utilized were an Ag/AgCl, 3 M NaCl electrode, and a platinum coil, respectively. Data acquisition and control were facilitated using a potentiostat/galvanostat Autolab system from EcoChemie. All electrochemical measurements were independently repeated multiple times (typically 6–7) to ensure reproducibility, and the presented data are representative of consistent experimental trends.

3. Results and discussion

3.1. Morphology and microstructure of CeO_2 films

SEM images corresponding to the PLD-grown $(CeO_2)_{UV}$ samples have been previously documented in another short communication.[14] Meanwhile, SEM images of $(CeO_2)_{0.5THe}$, $(CeO_2)_{2THe}$, and $(CeO_2)_{10mTO2}$, can be found in our earlier work.[19] To recap, CeO_2 films synthesized under vacuum exhibited a remarkably smooth surface, resembling the topography of a jigsaw puzzle. CeO_2 films grown in the presence of 0.5 Torr of helium comprised clusters of particles, while those produced under 2 Torr of helium displayed a fluffy-like texture. Additionally, CeO_2 films deposited in the presence of oxygen exhibited lamellae-like structures composed of particle clusters. Furthermore, XRD profiles of the CeO_2 films under consideration, along with estimations of crystallite size and lattice parameters, have been detailed in a separate publication.[19]

Low-resolution TEM images (Fig. S1) together with the HRTEM micrographs shown in Fig. 1 reveal a clear and progressive evolution in the nanostructure of PLD-grown CeO_2 as a function of background gas pressure and gas composition. In PLD, the kinetic energy of ablated species is largely determined by the number and type of gas-phase collisions occurring between the target and substrate; therefore, changes in deposition atmosphere directly influence nucleation behaviour, surface mobility, and resulting film morphology.[16,17] Under ultra-high vacuum (Fig. 1a), ablated Ce and Ce–O clusters experience very few collisions due to the extremely low gas density. As a result, the particles arrive at the substrate with comparatively high kinetic energy, which enhances their surface mobility and promotes the formation of well-dispersed nanocrystallites exhibiting clearly resolved fluorite-type CeO_2 lattice fringes. When 0.5 Torr of He is introduced (Fig. 1b), the mean free path shortens and ablated species undergo partial thermalization through frequent but low-energy collisions with the light He atoms. This moderates the kinetic energy of the arriving particles, promoting slightly larger grains and enhanced interparticle cohesion, while still preserving well-defined lattice contrast characteristic of high crystallinity. Increasing the He pressure to 2 Torr (Fig. 1c) further intensifies collisional scattering and facilitates gas-phase clustering of CeO_2 species before they reach the substrate. Consequently, more compact aggregates with extended crystalline domains are formed, reflecting the reduced impact energy and enhanced tendency for cluster coalescence in the plasma plume. In contrast to the inert He atmosphere, deposition under a mildly oxidative environment at 10 mT O_2 (Fig. 1d) introduces not only additional scattering events but also chemical interactions between ablated species and oxygen molecules. This combination yields the most uniform and densely packed nanocrystalline layer among all conditions studied, with continuous lattice fringes extending across larger regions. The SAED patterns presented in Fig. S2 fully support these observations, confirming that changes in gas pressure and composition during PLD systematically influence crystalline domain size, defect density, and overall nanocrystalline organization.

Raman spectroscopy offers qualitative insights into how oxygen vacancies affect the structure of CeO_2, particularly the oxygen sublattice. Although it does not directly quantify vacancy concentration, Raman analysis sensitively captures how defects modify vibrational modes and thus provides valuable clues about local structure and non-stoichiometry. Bulk CeO_2 exhibits well-defined Raman features including the F_{2g} mode at ~460–466 cm^{-1}, the 2 TA band, the defect-induced (*D*) mode, and the 2LO overtone with the F_{2g} mode being especially informative.[20] Because F_{2g} involves only oxygen motion, it serves as a direct indicator of lattice distortion arising from oxygen vacancies, stress, or grain-size effects. As summarized in Fig. 2, the PLD background atmosphere strongly influences these Raman signatures. The vacuum-grown film shows an F_{2g} mode at 466.3 cm^{-1} with a narrow FWHM of 9.6 cm^{-1}, closely matching the stoichiometric target and indicating high crystallinity with minimal defect content. The 0.5 Torr He film retains a similarly narrow FWHM (9.7 cm^{-1}) but exhibits a modest red shift to 462.8 cm^{-1}, consistent with the formation of a limited number of oxygen vacancies under low-pressure inert gas. Increasing the He pressure to 2 Torr produces a more pronounced red shift

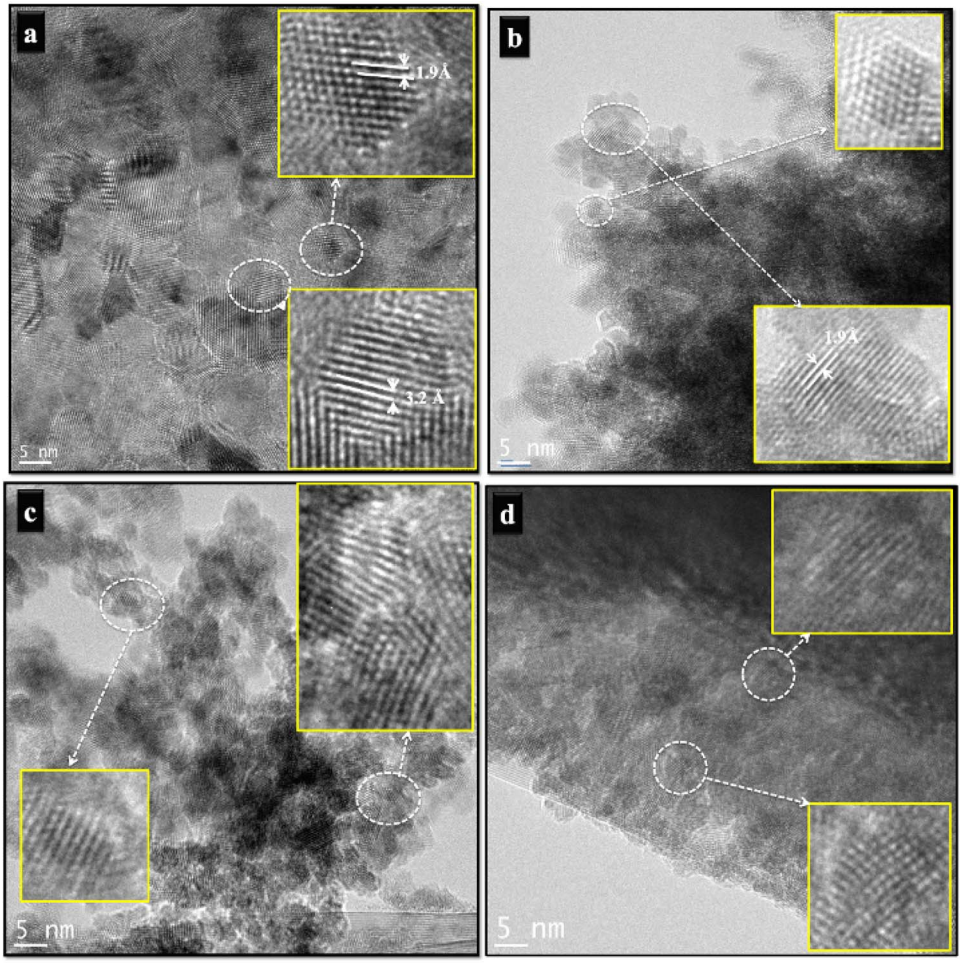

Fig. 1 HR-TEM images of PLD-grown CeO_2 film deposited on carbon paper under different atmospheres. (a) $(CeO_2)_{UV}$, (b) $(CeO_2)_{0.5THe}$, (c) $(CeO_2)_{2THe}$ and (d) $(CeO_2)_{10mTO2}$.

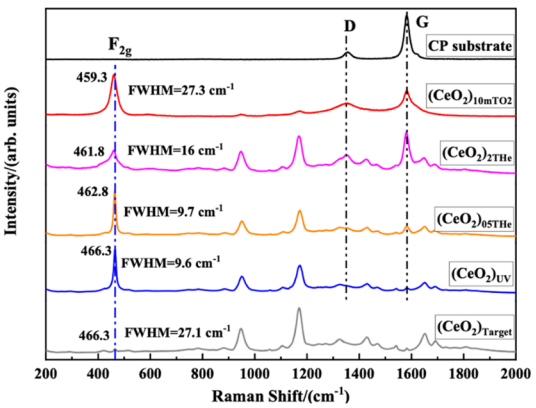

Fig. 2 Raman spectra of the stoichiometric CeO_2 PLD target and CeO_2 films deposited on carbon paper under different background atmospheres.

(461.8 cm^{-1}) and broader line width (16 cm^{-1}), reflecting enhanced lattice disorder and a higher vacancy density due to increased plume scattering and reduced oxygen incorporation. In contrast, CeO_2 deposited in 10 mTorr O_2 shows an even larger red shift (459.3 cm^{-1}) but a FWHM (27.3 cm^{-1}) nearly identical to the stoichiometric target. This combination suggests lattice relaxation associated with vacancy refilling while preserving high crystalline quality. Overall, the evolution of F_{2g} position and width across growth atmospheres reveals a clear structural progression: minimal vacancy content in vacuum, moderate non-stoichiometry at 0.5 Torr He, pronounced defect formation at 2 Torr He, and vacancy restoration under oxygen-rich conditions.

3.2. Surface redox chemistry and vacancy formation by XPS

XPS was utilized to analyze the composition and stoichiometry of CeO_2 films on the surface. Survey XPS scans of different CP/CeO_2 samples (Fig. S3) revealed the presence of C, O, and Ce elements. High-resolution Ce 3d XPS spectra (Fig. 3, left panel) reveal the coexistence of Ce^{4+} and reduced Ce^{3+} species across all PLD-grown films. Deconvolution of the Ce 3d envelope was performed using a Shirley background and Voigt line shapes; the canonical Ce^{4+} multiplet features (v, v'', v''' and u, u'', u''') and the lower-binding-energy Ce^{3+} satellites (v^0, v' and u^0, u') were

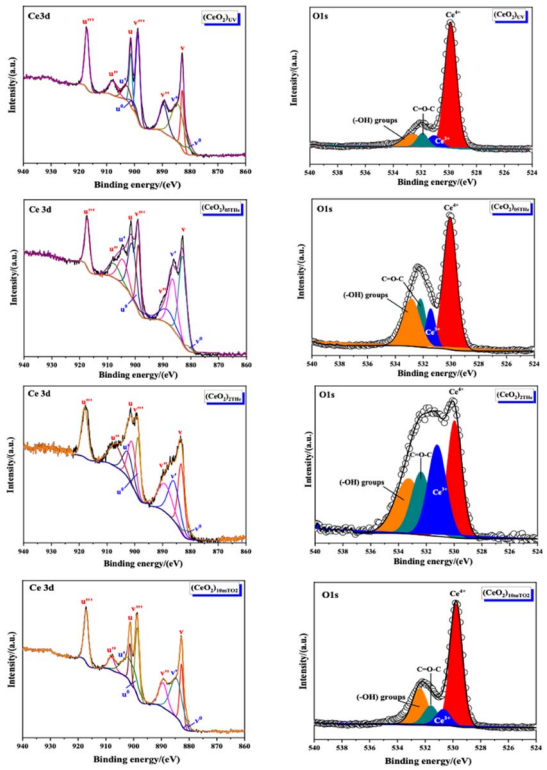

Fig. 3 High-resolution XPS core-level spectra of PLD-grown CeO_2 films deposited under different background atmospheres: left panel, Ce 3d spectra showing mixed Ce^{3+}/Ce^{4+} character; right panel, O 1s spectra deconvoluted into lattice oxygen, vacancy-associated oxygen, and surface adsorbate components.

constrained to consistent energy separations across samples.[21,22]

O 1s XPS spectra of CeO_2 films deposited under all four PLD conditions were deconvoluted into three components: lattice oxygen (O^{2-}), vacancy-associated oxygen bound to reduced cerium (Ce^{3+}–O_v), and higher-binding-energy contributions arising from surface hydroxyls and adsorbed species (Fig. 3, right panel). Films grown in helium atmospheres (0.5–2 Torr) exhibit a pronounced enhancement of the mid-binding-energy component, indicating an increased population of oxygen vacancies and defect-bound oxygen species. This effect is most evident for the 2 Torr He sample, consistent with its defect-rich microstructure inferred from Raman spectroscopy and TEM analysis. In contrast, films deposited under vacuum and 10 mTorr O_2 display a dominant lattice oxygen contribution and comparatively smaller vacancy- and adsorbate-related components, indicative of more ordered fluorite frameworks.

High-resolution Ce 3d spectra confirm the coexistence of Ce^{3+} and Ce^{4+} species in all samples (Table S1), reflecting the intrinsic redox flexibility of nanostructured ceria. The extracted Ce Ce^{3+}/Ce^{4+} ratios reveal that helium-assisted growth promotes significant electronic reduction, with the highest Ce^{3+} fraction observed for the 2 Torr He film ($Ce^{3+}/Ce^{4+} = 2.48$), followed by the 0.5 Torr He (2.34) and vacuum (1.96) samples. Deposition under 10 mTorr O_2 yields the lowest Ce^{3+}/Ce^{4+} ratio (1.30), consistent with partial re-oxidation of cerium cations in the presence of an oxygen background. These trends are in line with previous PLD studies demonstrating that background gas pressure and composition govern plume oxidation kinetics and defect stabilization in ceria films.[23,24]

Importantly, stoichiometric analysis based on O^{2-} and Ce atomic concentrations provides complementary insight into oxygen deficiency (Table S1). The lowest O^{2-} contents are found for the 0.5 Torr He and 2 Torr He samples (8.0% and 12.7%, respectively), yielding elevated [Ce]/[O^{2-}] ratios that reflect substantial anion vacancy formation. Although the 10 mTorr O_2 film exhibits the highest O^{2-} fraction (21.3%) and lowest [Ce]/[O^{2-}] ratio (1.68), it remains measurably non-stoichiometric, indicating that the supplied oxygen flux is insufficient to fully compensate for oxygen loss during ablation and film growth. The vacuum-deposited film occupies an intermediate regime, combining moderate Ce^{3+} content with limited oxygen depletion.

Taken together, the combined Ce 3d and O 1s analyses demonstrate that electronic reduction (Ce^{3+} formation) and oxygen vacancy concentration are correlated but not strictly proportional, reflecting the complex interplay between plume dynamics, gas-phase scattering, and surface re-oxidation during PLD. This defect landscape governs surface Lewis acidity, coordination unsaturation, and electronic polarizability in ceria,[25] parameters that are expected to critically influence enzyme adsorption, anchoring, and interfacial electronic communication in subsequent biohybrid electrode architectures.

3.3. XPS analysis of GOx immobilization on CeO_2 films

XPS is a well-established technique for evaluating protein adsorption and immobilization on solid supports,[26–29] and the survey spectra of CP/CeO_2/GOx (Fig. S4) clearly show a distinct N 1s peak at ~400.5 eV for all enzyme-treated samples, whereas nitrogen is absent in pristine CeO_2 (Fig. S3). Because CeO_2 contains no native nitrogen, the appearance of this N 1s signal provides direct evidence of GOx immobilization, reflecting nitrogen-bearing amino acid residues and functional groups. Quantification indicates nitrogen contents of 3.33, 5.66, 3.32, and 8.23 at% for $(CeO_2)_{UV}$, $(CeO_2)_{0.5THe}$, $(CeO_2)_{2THe}$, and $(CeO_2)_{10mTO2}$, respectively, with the higher values for the 2 Torr He and 10 mT O_2 films suggesting more extensive enzyme loading. High-resolution C 1s and O 1s spectra display multiple components consistent with the complex chemical environment of the protein, though detailed deconvolution is beyond the scope of this study. Importantly, part of the N 1s intensity originates from the flavin adenine dinucleotide (FAD) cofactor within GOx.

High-resolution N 1s spectra of CeO_2/GOx (Fig. 4) deconvolute into two components: a H–N feature (≈400.0 eV) assigned to amide/amine nitrogen in the GOx polypeptide and a =N– feature (≈401.0 eV) consistent with heterocyclic nitrogen in the FAD isoalloxazine ring.[30] Quantitatively, the H–N/=N peak-area ratios are 1.20, 1.25, 1.07 and 1.24 for the UV, 0.5 Torr He, 2 Torr He and 10 mTorr O_2 samples, respectively, corresponding to =

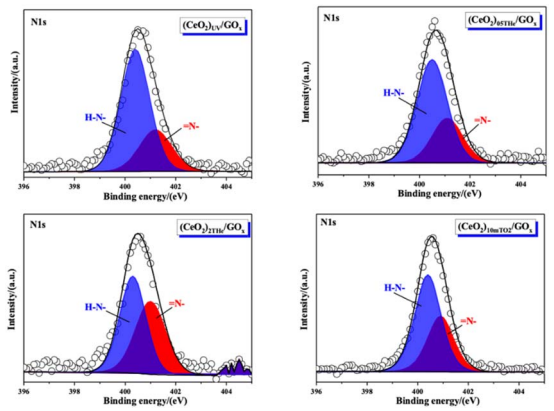

Fig. 4 High-resolution N 1s XPS spectra of CeO_2/GOx electrodes showing two components assigned to amide/amine nitrogen (H–N, ~400.0 eV) from the GOx polypeptide backbone and heterocyclic nitrogen (=N–, ~401.0 eV) associated with the flavin adenine dinucleotide (FAD) cofactor.

N contributions of ≈45.5%, 44.4%, 48.3% and 44.6% of the N 1s envelope. The near-parity of the two components, particularly for the 2 Torr He sample indicates a substantial contribution from FAD-derived nitrogen in the surface ensemble and supports the conclusion that the FAD cofactor remains associated with immobilized GOx. We stress that XPS reports ensemble surface chemistry and cannot unambiguously assign a single atomic origin; nevertheless, the observed binding energy positions and area proportions are fully consistent with amide/amine backbone nitrogen and FAD isoalloxazine =N contributions.[31] Thus, the observed N 1s peak not only verifies enzyme immobilization but also implies retention of GOx's critical structural motifs, including the nitrogen-containing FAD cofactor responsible for catalytic turnover.

While the N 1s signal confirms the presence of GOx-derived nitrogen species on the CeO_2 surface, XPS does not provide information on the structural integrity or catalytic activity of the immobilized enzyme. The electrochemical activity of the immobilized enzyme was further verified by cyclic voltammetry in the absence of glucose (Fig. S8), confirming the presence of a redox-active GOx layer, as discussed below.

3.4. Bioelectrocatalytic activity

Due to its inherent insulating nature at room temperature, pure CeO_2 does not readily facilitate the electron transfer processes required for typical electrochemical reactions in an electrolyte like PBS. CeO_2 is frequently used as a support material for other electrochemically active components (*e.g.*, noble metal nanoparticles or conductive carbon phases).[32] In these composite materials, the other component provides the necessary conductivity, while the CeO_2 offers catalytic active sites, often through its unique redox properties (Ce^{4+}/Ce^{3+} transition) and oxygen vacancies.

Fig. S5 presents the cyclic voltammogram (CV) of the bare carbon paper (CP) substrate recorded in PBS solution. The measured current densities remain very low over the potential window from −0.45 to 0.60 V *vs.* Ag/AgCl, confirming the essentially electrochemically inert behavior of the CP substrate within this range. Nevertheless, a weak anodic peak is observed at approximately 0.088 V, accompanied by a corresponding cathodic feature at around 0.137 V. These redox features are attributed to the reversible oxidation and reduction of surface oxygen-containing functional groups on the carbon paper, which originate from pre-existing surface oxides formed upon exposure to ambient oxygen.

All CeO_2-modified electrodes (Fig. S6) exhibit higher current densities than the bare CP substrate (Fig. S5), confirming that the CeO_2 overlayer dominates the electrochemical response. Redox-like features associated with surface Ce^{3+}/Ce^{4+} transitions are present on all CeO_2 electrodes; however, they are most well-defined for the film deposited under 2 Torr He with peak positions at approximately 0.10 and 0.027 V. For the other electrodes (vacuum, 0.5 Torr He, 10 mTorr O_2), the Ce^{3+}/Ce^{4+} signals are broader and less pronounced, yet the elevated current relative to bare CP (Fig. S5) indicates significant defect-related redox activity. The more distinct peaks in the 2 Torr He sample are attributed to its higher concentration of oxygen vacancies and reduced cerium species, as independently confirmed by Raman spectroscopy and XPS. These results highlights the critical role of deposition atmosphere in tuning the defect chemistry and the electrochemical accessibility of Ce^{3+}/Ce^{4+} surface states.

In PBS containing glucose, the cyclic voltammograms of all CeO_2-modified electrodes display profiles that closely resemble those recorded in PBS alone (Fig. S7). The addition of glucose does not introduce new redox features: the peak positions remain identical to those observed in glucose-free PBS, and in several cases the overall current density is even lower than in the corresponding PBS measurements. This behavior indicates that glucose does not participate in any detectable faradaic reaction at these CeO_2 films. Importantly, CeO_2 is not recognized as an electrocatalyst for glucose oxidation in neutral media, and the present results remain fully consistent with this expected inactivity. Even the defect-rich CeO_2 synthesized at 2 Torr He, despite showing more pronounced features in PBS fails to exhibit any glucose-specific response. Taken together, the CVs confirm that the observed signals originate solely from the underlying capacitive and defect-related redox behavior of the CeO_2/carbon paper system, with no measurable electrocatalytic oxidation of glucose under the conditions tested. The absence of any glucose-related electrochemical response at CeO_2 electrodes in the absence of GOx further confirms that CeO_2 itself does not catalyze glucose oxidation, and therefore that the catalytic signals observed for CeO_2–GOx electrodes arise from the enzymatic activity of immobilized GOx.

To assess the electrochemical activity of the immobilized enzyme independently of substrate oxidation, cyclic voltammetry was performed in the absence of glucose (Fig. S8). All CeO_2–GOx electrodes exhibit well-defined redox features with formal potentials ($E^{o\prime}$ = (Epa + Epc)/2) of 0.464 V, 0.457 V, and 0.461 V *vs.* Ag/AgCl for $(CeO_2)_{UV}$–GOx, $(CeO_2)_{0.5THe}$–GOx, and $(CeO_2)_{2THe}$–GOx, respectively. These values are in excellent agreement with the reported potential of the FAD/$FADH_2$ redox

couple of glucose oxidase, confirming that the enzyme remains structurally intact and electrochemically active upon immobilization. The narrow potential dispersion across different CeO_2 nanostructures further indicates a robust and reproducible bioelectronic interface. Data for $(CeO_2)_{10mTO2}$–GOx could not be included due to data unavailability; however, its catalytic behavior follows the same trends discussed below.

Upon addition of glucose, a pronounced increase in current is observed (Fig. 5), as discussed below. When recorded at varying scan rates in PBS containing glucose, the voltammograms exhibit a well-defined catalytic anodic wave for every CeO_2–GOx sample, a feature that is entirely absent in both the bare CeO_2 and CeO_2/CP control electrodes. The catalytic current increases linearly with scan rate, consistent with a surface-confined, enzyme-mediated redox process associated with the $FAD/FADH_2$ active center of GOx, rather than diffusion-controlled behavior.

Further insight is provided by the analysis of the formal potential $E^{\circ\prime}$, extracted at different scan rates. As shown in the upper-right panels of Fig. 5, the formal potentials for all CeO_2–GOx electrodes fall within a narrow range of 0.45–0.46 V *vs.* Ag/AgCl, in excellent agreement with the reported $FAD/FADH_2$ redox potential of GOx under physiological pH conditions.[33] Importantly, the formal potential remains essentially invariant with scan rate and deposition atmosphere, indicating a well-defined, surface-confined redox couple with minimal kinetic distortion. This behavior confirms that the observed redox signatures originate from the immobilized enzyme and are not associated with CeO_2 or the carbon paper substrate. The preservation of a constant formal potential further suggests that GOx retains its native electrochemical characteristics upon immobilization, with CeO_2 acting primarily as an efficient structural and electronic interface rather than perturbing the intrinsic thermodynamics of the FAD cofactor. The small anodic peak-to-cathodic peak separation (ΔEp) and the near-symmetry between anodic and cathodic peak currents indicate a rapid and highly reversible electron-transfer kinetics. Such behavior is characteristic of fast interfacial processes and provides strong evidence for DET-like communication between the $FAD/FADH_2$ redox center of GOx and the CeO_2-modified electrode. These results confirm that the electrocatalytic response arises from the enzymatically active cofactor, with CeO_2 acting as an efficient electronic and structural interface rather than contributing directly to the catalytic process.

It is important to distinguish this behavior from classical mediated electron transfer (MET), where diffusional redox mediators shuttle electrons between the enzyme and the electrode. In the present system, no external mediator is present, and the observed response instead arises from direct electronic coupling between the $FAD/FADH_2$ center of GOx and the redox-active CeO_2 interface.

3.5. Charge storage properties of CeO_2/GOx bio-hybrid electrodes

The CeO_2/GOx bio-hybrid electrodes exhibit a composite electrochemical response arising from the interplay between pseudocapacitive charge storage in nanostructured ceria and faradaic enzymatic processes associated with surface-immobilized GOx (Fig. 5). The capacitive component originates from fast and reversible Ce^{4+}/Ce^{3+} surface redox transitions enabled by oxygen vacancies, giving rise to pseudocapacitive behavior characteristic of non-stoichiometric ceria. In parallel, the immobilized enzyme contributes a faradaic component associated with the $FAD/FADH_2$ redox couple,

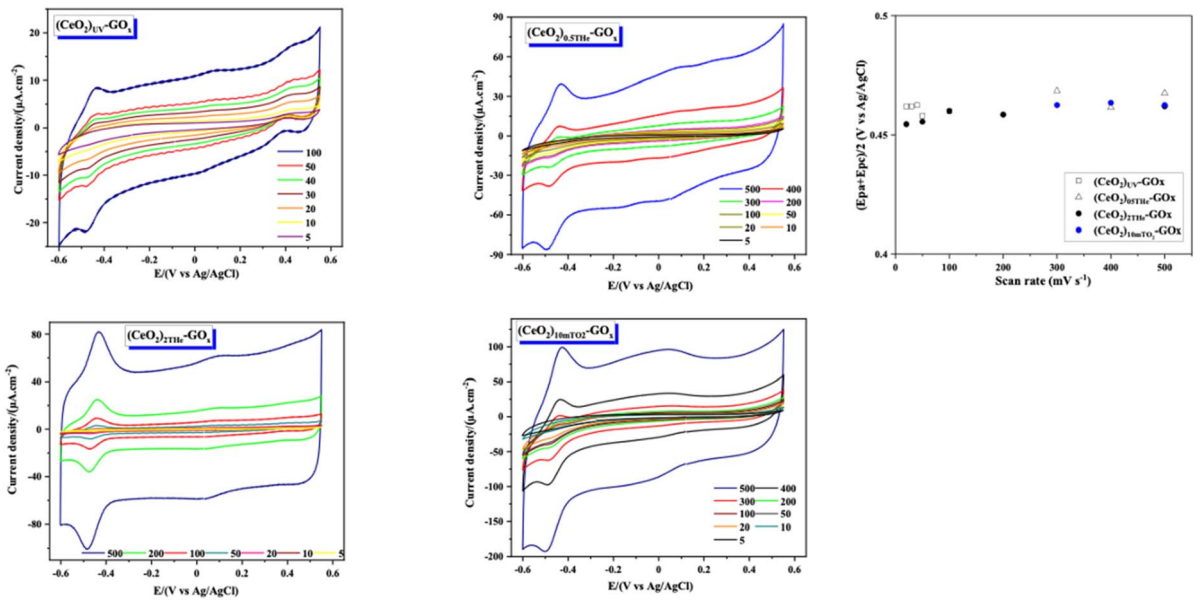

Fig. 5 Cyclic voltammograms of CeO_2/GOx biohybrid electrodes recorded in PBS containing 4 mM glucose at different scan rates. Scan rates (mV s^{-1}) are visible in the legend. (Left panel) The CVs correspond to CeO_2 films deposited under different PLD atmospheres, as indicated in each graph. (Right panel) Formal potential, $E^{\circ\prime} = (Epa + Epc)/2$.

which becomes catalytically active in the presence of glucose. Enzyme-assisted charge accumulation has been previously reported in redox–protein interfaces, where flavin cofactors can transiently participate in interfacial electron buffering and give rise to measurable quasi-capacitive responses rather than classical double-layer charging alone.[33–36]

The specific capacitance derived from the CV curves, is calculated using the formula $C_p = Q/(2\ A \times \nu \times \Delta V)$. In this equation, Q (A V) is the voltametric charge obtained by integrating the areas of both oxidation and reduction on the CV curve, A (cm^2) is geometric area of the working electrode, ν is the scan rate (V s^{-1}), and ΔV (V) indicates the potential window of the CV. All four biohybrid electrodes display the expected decay in C_p with increasing scan rate, consistent with diffusion-limited charge propagation and partial loss of electroactive accessibility at higher scan rates (Fig. 6). Nevertheless, clear differences emerge as a function of the PLD atmosphere used for forming the CeO_2 scaffold. At low scan rates, $(CeO_2)_{10mTO2}$/GOx exhibits the highest apparent capacitance, reaching >0.6 mF cm^{-2} at 5 mV s^{-1}, consistent with facile electrolyte polarization at its comparatively oxygen-rich surface. In contrast, $(CeO_2)_{UV}$/GOx and $(CeO_2)_{0.5THe}$/GOx show modest but more scan-rate stable values in the 50–200 mV s^{-1} range, whereas $(CeO_2)_{2THe}$/GOx presents the lowest C_p at slow scan rates but undergoes a progressive recovery above 200 mV s^{-1}, surpassing both the $(CeO_2)_{UV}$/GOx and $(CeO_2)_{0.5THe}$/GOx films at the highest scan rates conditions. This behavior supports a biohybrid interfacial mechanism in which CeO_2 acts as a redox-active, pseudocapacitive scaffold that rapidly buffers and redistributes charge *via* Ce^{4+}/Ce^{3+} transitions, while the immobilized GOx layer introduces a glucose-dependent faradaic pathway through the FAD/$FADH_2$ redox center. The coupling between these processes results in a hybrid response where pseudocapacitive charge storage and enzymatic catalysis coexist but remain electrochemically distinguishable: the CeO_2 contribution dominates the capacitive background, whereas the enzyme introduces a catalytic current that increases upon glucose addition. Such behavior is consistent with previous reports on hybrid bioelectrochemical systems, where protein films influence apparent capacitance by transiently accommodating electronic charge at the electrode–electrolyte interface.[27,34–37] Importantly, in the absence of glucose, only the surface-confined FAD/$FADH_2$ redox couple is observed, whereas the catalytic current emerges exclusively upon glucose addition, further confirming the enzymatic origin of the faradaic response and clearly differentiating it from the pseudocapacitive contribution of the CeO_2 scaffold.

Altogether, these results indicate that defect-engineered ceria can couple oxide-based pseudocapacitance with enzyme-assisted interfacial redox buffering in a single CeO_2/GOx architecture. While further *operando* and time-resolved studies will be required to fully resolve the charge-transfer pathways, the present findings demonstrate that oxidase-based bio-hybrid films can simultaneously support biocatalytic activity and measurable charge storage. This dual functionality is particularly attractive for biosensing and enzymatic energy-conversion platforms, where enhanced interfacial coupling is expected to improve signal stability, charge utilization, and power delivery under dynamic operating conditions.[2,34,35]

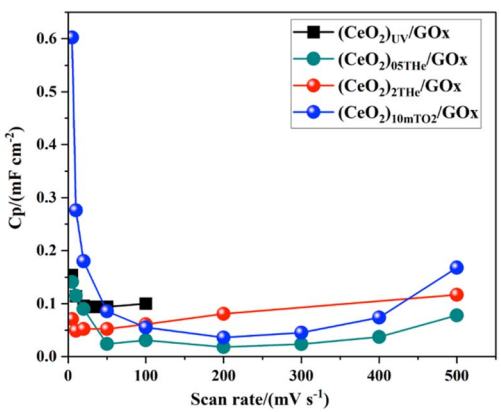

Fig. 6 Apparent specific capacitance (*Cp*) of CeO_2/GOx biohybrid electrodes as a function of scan rate in PBS containing glucose. C_p values were extracted from cyclic voltammograms of Fig. 5 recorded at different scan rates for CeO_2 films deposited under the PLD atmospheres indicated in the legend.

4. Conclusion

Raman and XPS analyses consistently demonstrate that the background atmosphere during pulsed laser deposition plays a decisive role in governing the defect chemistry and stoichiometry of CeO_2 films. Helium-rich environments, particularly at 2 Torr, promote oxygen-vacancy formation through enhanced plume scattering and limited oxygen incorporation, resulting in elevated Ce^{3+} fractions, broadened Raman F_{2g} modes, and pronounced vacancy-related O 1s components. In contrast, films deposited under ultra-high vacuum or low O_2 partial pressure exhibit more ordered fluorite lattices with comparatively reduced defect signatures.

CeO_2 itself does not catalyze glucose oxidation, ensuring that the observed electrocatalytic response arises exclusively from the immobilized biorecognition element. Upon GOx immobilization, all CeO_2–GOx electrodes display well-defined catalytic waves absent in enzyme-free controls. The scan-rate-dependent surface-confined kinetics, invariant formal potentials closely matching the FAD/$FADH_2$ redox couple, and small peak-to-peak separations are all consistent with efficient direct electron transfer between GOx and the CeO_2-modified electrode, achieved without soluble mediators or conductive nanocarbon additives.

To further distinguish between capacitive and faradaic contributions, the capacitive component is attributed to fast and reversible Ce^{4+}/Ce^{3+} surface redox transitions within nanostructured CeO_2, which are characteristic of pseudocapacitive charge storage. In contrast, the faradaic contribution arises from the redox activity of the FAD/$FADH_2$ cofactor of the immobilized glucose oxidase (GOx), which drives glucose oxidation.

Importantly, these two processes are intrinsically coupled rather than independent. The redox-active CeO_2 scaffold

functions as a dynamic charge buffer, transiently accommodating and redistributing electrons during enzymatic turnover. This behavior facilitates efficient electronic communication between the enzyme and the electrode, thereby enhancing the overall electrochemical response.

This interpretation is supported by (i) control experiments performed on CeO_2 electrodes in the absence of GOx, which exhibit no catalytic response toward glucose, (ii) the observation of the characteristic FAD/$FADH_2$ redox couple associated with the immobilized enzyme, and (iii) the clear increase in current upon glucose addition. The revised manuscript now explicitly emphasizes this coupled bioelectrochemical mechanism.

Although the present study emphasizes fundamental interfacial electrochemistry rather than device-level metrics, the results identify defect-rich CeO_2 as a promising oxide platform for mediator-free bioelectronic interfaces. Future efforts will focus on translating these CeO_2–enzyme architectures into practical optimization of the biosupercapacitor biosensing and enzymatic biofuel cell configurations, where the combination of defect-mediated redox activity, enzyme compatibility, and simplified electrode design may offer advantages in stability, scalability, and material sustainability.

This pseudocapacitive charge buffering is not merely a parallel phenomenon but plays an active role in modulating the enzyme–electrode interface, by transiently accommodating and redistributing electronic charge during enzymatic turnover. Such coupling between oxide redox chemistry and enzyme activity provides a distinct functional advantage compared to conventional bioelectrodes lacking intrinsic charge storage capability.

Conflicts of interest

There are no conflicts to declare.

Data availability

Data will be made available on request. Supplementary information (SI) is available. See DOI: https://doi.org/10.1039/d6ra01081d.

Acknowledgements

The authors acknowledge the support the financial support provided by the Natural Sciences Engineering Research Council of Canada (NSERC) through the Discovery Grant and the Quebec Centre for Advanced Materials (QCAM).

References

1 S. U. Haque, N. Duteanu, S. Ciocan and A. Nasar, Inamuddin, *J. Environ. Manag.*, 2021, **298**, 113483, DOI: 10.1016/j.jenvman.2021.113483.
2 X. Xiao, H. Q. Xia, R. Wu, L. Bai, L. Yan, E. Magner, S. Cosnier, E. Lojou, Z. Zhu and A. Liu, *Chem. Rev.*, 2019, **119**, 9509–9558, DOI: 10.1021/acs.chemrev.9b00115.
3 S. Prabhulkar, H. Tian, X. Wang, J. J. Zhu and C. Z. Li, *Antioxid. Redox Signaling*, 2012, **17**, 1796–1822, DOI: 10.1089/ars.2011.4001.
4 R. D. Milton and S. D. Minteer, *J. R. Soc. Interface*, 2017, **14**, 20170253, DOI: 10.1098/rsif.2017.0253.
5 J. A. Bauer, M. Zámocká, J. Majtán and V. Bauerová-Hlinková, *Biomolecules*, 2022, **12**, 472, DOI: 10.3390/biom12030472.
6 J. Liu, A. Chou, W. Rahmat, M. N. Paddon-Row and J. J. Gooding, *Electroanalysis*, 2005, **17**, 38–46, DOI: 10.1002/elan.200403116.
7 M. M. Rahman, A. J. S. Ahammad, J. H. Jin, S. J. Ahn and J. J. Lee, *Sensors*, 2010, **10**, 4855–4886, DOI: 10.3390/s100504855.
8 J. P. Ball, B. A. Mound, A. G. Monsalve, J. C. Niño and J. B. Allen, *J. Biomed. Mater. Res., Part A*, 2014, **102**, 1778–1785, DOI: 10.1002/jbm.a.35137.
9 C. Xu and X. Qu, *NPG Asia Mater.*, 2014, **6**, e90, DOI: 10.1038/am.2013.88.
10 C. Korsvik, S. Patil, S. Seal and W. T. Self, *Chem. Commun.*, 2007, 1056–1058, DOI: 10.1039/B615134E.
11 E. G. Heckert, A. S. Karakoti, S. Seal and W. T. Self, *Biomaterials*, 2008, **29**, 2705–2709, DOI: 10.1016/j.biomaterials.2008.03.014.
12 P. R. Solanki, C. Dhand, A. Kaushik, A. A. Ansari, K. N. Sood and B. D. Malhotra, *Sens. Actuators, B*, 2009, **141**, 551–556, DOI: 10.1016/j.snb.2009.05.034.
13 S. Deshpande, S. Patil, S. V. N. T. Kuchibhatla and S. Seal, *Appl. Phys. Lett.*, 2005, **87**, 133113, DOI: 10.1063/1.2061873.
14 M. Moumene, A. Tabet-Aoul, M. Gougis, D. Rochefort and M. Mohamedi, *Int. J. Electrochem. Sci.*, 2014, **9**, 176–184, DOI: 10.1016/S1452-3981(23)07706-4.
15 G. K. Hubler, in *Pulsed Laser Deposition of Thin Films*, ed. D. B. Chrisey and G. K. Hubler, John Wiley & Sons, New York, 1994, pp. 327–355.
16 R. Eason, *Pulsed Laser Deposition of Thin Films: Applications-Led Growth of Functional Materials*, John Wiley & Sons Ltd, Hoboken, USA & Chichester, UK, 2006.
17 N. A. Shepelin, Z. P. Tehrani, N. Ohannessian, C. W. Schneider, D. Pergolesi and T. Lippert, *Chem. Soc. Rev.*, 2023, **52**, 2294–2321, DOI: 10.1039/D2CS00938B.
18 E. Irissou, F. Vidal, T. Johnston, M. Chaker, D. Guay and A. N. Ryabinin, *J. Appl. Phys.*, 2006, **99**, 034904, DOI: 10.1063/1.2165412.
19 M. Gougis, A. Tabet-Aoul, D. Ma and M. Mohamedi, *Microchim. Acta*, 2014, **181**, 1207–1214, DOI: 10.1007/s00604-014-1283-9.
20 S. Wang, W. Wang, J. Zuo and Y. Qian, *Mater. Chem. Phys.*, 2001, **68**, 246–250, DOI: 10.1016/S0254-0584(00)00357-6.
21 S. Mofarah, E. Adabifiroozjaei, Y. Yao, *et al.*, *Nat. Commun.*, 2019, **10**, 2594, DOI: 10.1038/s41467-019-10621-2.
22 K. Zhuang, P. Jin, L. Yang, J. Yao, L. Yu, Z. Sheng, X. Chu, Z. Zhuang and X. Chen, *RSC Adv.*, 2023, **13**, 25989–25997, DOI: 10.1039/D3RA03018K.
23 P. R. Willmott and J. R. Huber, *Rev. Mod. Phys.*, 2000, **72**, 315–328, DOI: 10.1103/RevModPhys.72.315.
24 W. Mao, W. Gong, Z. Gu, M. Wilde, J. Chen, K. Fukutani, H. Matsuzaki, B. Fugetsu, I. Sakata and T. Terai, *Int. J.*

Hydrogen Energy, 2024, **50**, 969–978, DOI: 10.1016/j.ijhydene.2023.08.264.

25 T. Montini, M. Melchionna, M. Monai and P. Fornasiero, *Chem. Rev.*, 2016, **116**, 5987–6041, DOI: 10.1021/acs.chemrev.5b00603.

26 D. Addari, A. Mignani, E. Scavetta, D. Tonelli and A. Rossi, *Surf. Interface Anal.*, 2011, **43**, 816–822, DOI: 10.1002/sia.3636.

27 D. Ivnitski, K. Artyushkova, R. A. Rincón, P. Atanassov, H. R. Luckarift and G. R. Johnson, *Small*, 2008, **4**, 357–364, DOI: 10.1002/smll.200700725.

28 S. Libertino, A. Scandurra, V. Aiello, M. Fichera, F. Sinatra and M. Renis, *Appl. Surf. Sci.*, 2007, **253**, 9116–9123, DOI: 10.1016/j.apsusc.2007.05.039.

29 A. Griffith, A. Glidle and J. M. Cooper, *Biosens. Bioelectron.*, 1996, **11**, 625–631, DOI: 10.1016/0956-5663(96)83297-0.

30 R. J. J. Jansen and H. van Bekkum, *Carbon*, 1995, **33**, 1021–1027, DOI: 10.1016/0008-6223(95)00030-H.

31 G. Lu, H. Zheng, J. Lv, G. Wang and X. Huang, *J. Power Sources*, 2020, **480**, 229091, DOI: 10.1016/j.jpowsour.2020.229091.

32 H. T. Das, T. E. Balaji, S. Dutta, N. Das, P. Das, A. Mondal and M. Imran, *J. Energy Storage*, 2022, **50**, 104643, DOI: 10.1016/j.est.2022.104643.

33 D. Ivnitski, B. Branch, P. Atanassov and C. Apblett, *Electrochem. Commun.*, 2006, **8**, 1204–1208, DOI: 10.1016/j.elecom.2006.05.024.

34 J. Lee, S. Han and Y. Kwon, *Chem. Eng. J.*, 2024, **487**, 150557, DOI: 10.1016/j.cej.2024.150557.

35 D. Pankratov, P. Falkman, Z. Blum and S. Shleev, *ChemElectroChem*, 2014, **1**, 1798–1807, DOI: 10.1002/celc.201402158.

36 Y. Zhang, H. Deng, Y. Zheng, C. Li, Y. Long, Z. Li, W. Xu and G. Li, *J. Energy Storage*, 2024, **82**, 110604, DOI: 10.1016/j.est.2024.110604.

37 S. Shleev, *et al.*, *Bioelectrochemistry*, 2005, **67**, 115–120, DOI: 10.1016/j.bioelechem.2005.02.004.